Moose Project

Part 2

Vaughn Ramsey

March 2025

1 Introduction

In order to introduce well founded regulation for nuclear fuel it is important to have a robust computational modeling framework that accurately predicts the thermal and mechanical behavior of the fuel elements in question. In part one of this project we introduced a one dimensional heat transport model to examine the thermal properties of a UO_2 fuel pellet, with a Helium gap and $Zr4$ cladding. In this study we will extend the model to a 1[m] smeared pellet 2D model. While this project will not provide sufficiently comprehensive modeling inform actual regulation, it is important for developing our understanding of computational methods that reflect analytical and observed phenomena. Key to this process is the mesh refinement studies which provide confidence that the computational model is effectively capturing analytical and observed behaviors. Finding a well defined mesh, we utilize MOOSE to simulate the fuel element under a steady state as well as a transient. The axial temperature profiles are observed and reported under both circumstances.

2 Setup and Mesh Refinement

2.1 Material Properties and Model

To model our 1-D simulation we begin by finding material properties in the literature.[1-7] For our mesh convergence study in 1-D we start by finding material properties in literature. The relevant material properties are listed in Table 1. Table 2.

Material	Specific Heat (J/kg·K)	Density (kg/cm^3)
UO_2 (Fuel)	296.7	0.01097
Helium (Gap)	5190	0.000000164
Zircaloy-4 (Cladding)	2850	0.00656

Table 1: Utilized specific heat and density values for UO_2, helium, and Zircaloy-4. Some values were lightly modified from sources in literature.

Material	Thermal Conductivity Model (W/cm·K)
UO_2	$k = \frac{1}{2(1.48+0.04\max(T,300))}$
Helium	$k = 0.0025 + 0.00002T$
Zircaloy-4	$k = 0.18 - 0.00002T$

Table 2: Temperature-dependent thermal conductivity models for UO_2, helium, and Zircaloy-4. Temperature (T) is in Kelvin. Again, some coefficients were lightly modified from values in literature.

These functions were defined in the functions block and referenced in each heat conduction material's thermal conductivity temperature function. Auxiliary variables and kernels were set up so that the thermal conductivity can be checked at different points in the material and at different times (in the transient simulation).

In the 1-D case a heat conduction kernel is implemented with a volumetric heating rate of $q = \frac{350}{0.25\pi}$, derived from the $LHR = 350\frac{[\text{W}]}{[\text{cm}]}$ given in the problem statement. This volumetric heating rate will redefined to vary axially, and again temporally in the latter stages of implementation. In addition, two boundary conditions were implemented, a Dirichlet boundary condition for constant coolant temperature in the 1-D case - convective cooling BC in the 2-D case - and a Neumann boundary condition in all models, to prevent heat transfer across the centerline of the rod.

2.2 1-D Refinement

To start building our mesh we consider the basics of the problem, building out from a 1-D mesh. We recognize that it is important to have nodes located at the interface of each material and on the corners of our model. To achieve this we define 3 generated meshes, one on the domain $x \in [0, 0.5], y \in 0, 0.1$ for the fuel, one on $x \in [0.5, 0.505], y \in [0, 0.1]$ for the gap, and one on $x \in [0.505, 0.605], y \in [0, 0.1]$. We start by meeting the minimum mesh requirements with an n_x of 3, which yields one solid block on each subdomain. Then we use the stitched mesh generator to combine our generated meshes, and finally the subdomain bounding box generator to redefine out subdomains that were lost in the stitching. This yields the mesh we see in the simulation depicted in Fig. 1.

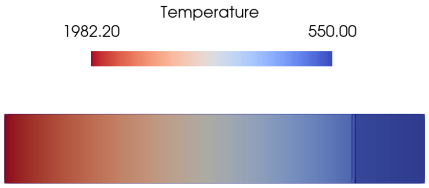

Figure 1: Heat map for simulated fuel rod with $n_x = 3$

[H] We can clearly see that the heat is uniformly diffusing across the fuel element. To resolve this numerical inaccuracy, we need to refine our mesh. In order to systematically control the mesh refinement process, I incrementally increased the number of subdivisions uniformly across each component, so that for $n_x = 9$, there are three nodes in the fuel, three across the gap, and three across the clad. Through this process, I began slowly increasing the number of subdivisions, then taking larger steps as convergence slowed, until we reached a sufficiently small change in center-line temperature between iterations in mesh refinement. The general refinement process can be seen in Fig. 2.

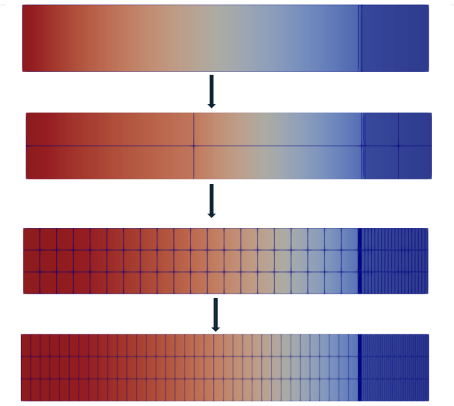

Figure 2: Abstracted flowchart of the mesh refinement process.

This ultimately yielded a change in temperature of $\Delta T_0 = 0.04^o K$ for an increase of 1 in n_x. We reached this tolerance at $n_x = 102$, or 35 subdivisions across each material (i.e. fuel, gap, clad). See a plot of our convergence by ΔT_0 vs n_x in Fig. 3.

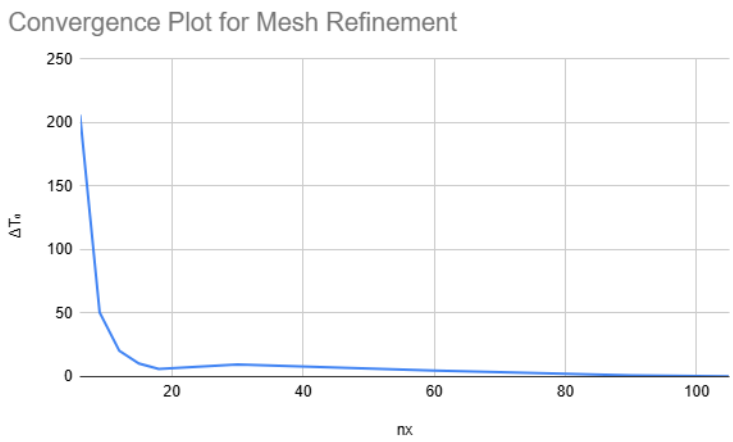

Figure 3: Convergence plot of change in center-line temperature as mesh is refined.

Not having a specified tolerance, I chose to stop here, as further refinement slowed the convergence of our thermal conductivity solver without yielding large improvements in calculated center-line temperature.

2.2.1 1-D Results

For our 1-D mesh refinement study in the solid state case we found a centerline temperature $T_0 \approx 1590$ K. This was close to the analytical solution for the steady state heat profile. Transient simulations were also performed but the steady-state results are far more helpful for validating the accuracy of our extension into 2-D. For the sake of completeness we will show the transient data ($LHR(t) = 350 \cdot e^{-\frac{(t-20)^2}{2}} + 350$, defined in the problem statement) so that the steady-state solution can be observed after recovery (e.g. $t = 80$[s] Find the results for the transient 1-D simulations shown in Fig. 4.

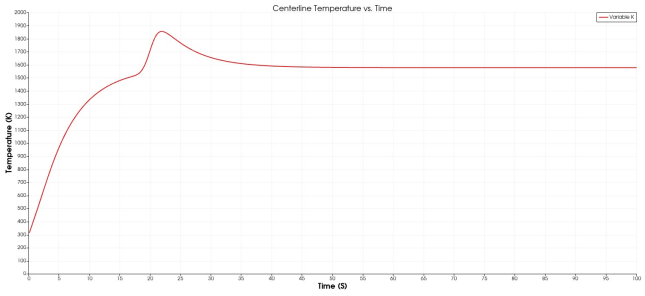

Figure 4: Centerline temperature vs. time for 1-D simulation of fuel pellet undergoing transient.

2.3 2-D Refinement

The 2-D refinement study is very similar to the 1-D case. The y component of the subdomains is extended to $1m$, then the model is solved for various n_y values and the solutions are compared. To make it physically representative we implemented an LHR that varies axially

$$q(y) = \frac{\left(350 \cdot \cos\left(1.2 \cdot \left(\frac{y}{50} - 1\right)\right)\right)}{0.25 \cdot \pi}$$

We also implement a convective cooling boundary condition using the equation covered in class. T_∞ is defined axially by the equation:

$$T_\infty(y) = 500 + \frac{1}{1.2} \cdot \frac{50 \cdot 350}{(.085 \cdot 4180) \cdot (\sin(1.2) + \sin(1.2 \cdot ((\frac{y}{50}) - 1))}$$

The coolant specific heat, and flow rate values were determined to be reasonable compared to reported values in literature.[8,9] A bash script was implemented to automate the refinement study increasing n_y by increments of 10 from 10 to 110. The results of this study are seen in Figure 5.

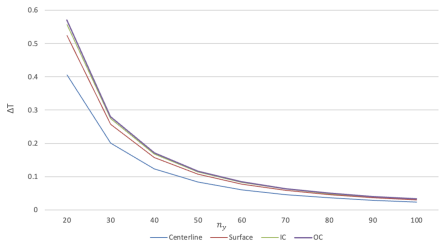

Figure 5: Residual convergence plot for mesh refinement in y direction.

The residual convergence (ΔT) was found through the following equation:

$$\Delta T(n_y) = \int_0^{100} \left| T_{n_y}(y) - T_{n_y - 1}(y) \right| dy$$

Numerically, the residual convergence was computed as a Riemann sum with $\Delta y = \frac{1}{1000}$. The residual convergence alone appears to display favorable convergence behavior after $n_y \approx 50$ with $\Delta T \approx 0.1$, we observe further convergence to $\Delta T \approx 0.025$ K without significantly slowing the solver at $n_y = 100$. Given the lack of solver convergence at such a high refinement, $n_y = 100$ was determined to be sufficient refinement. One other reason for this is the aspect ratio of the elements. It is established that in finite element analysis large aspect ratios can introduce error into the solver.[10] Under $n_y = 10$ our aspect ratio $a = 68,000$, but increasing n_y to 100 gives us an aspect ratio of $6,800$. Improving our aspect ratio by an order of magnitude promises to help mitigate the error of our numerical solver. It should be noted that in the 2-D refinement we operated in a constant step of y_n of 10, so the values of ΔT here overestimate the actual convergence behavior.

3 Steady State Simulation

To solve the temperature profile along this 2-D smeared pellet model, this model was ultimately the result of our final refined mesh. We observe the axial temperature profiles at key points in the fuel element in Fig. 6.

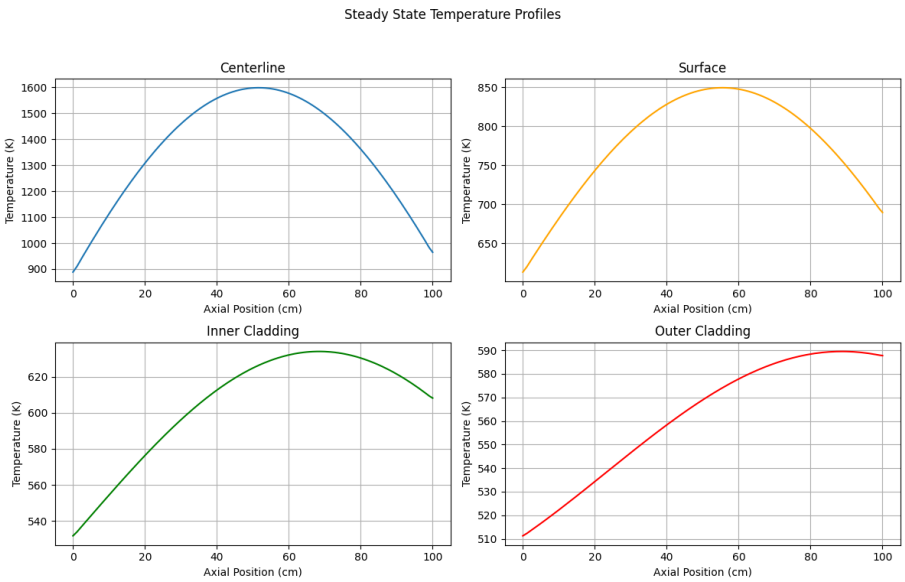

Figure 6: Axial temperature profiles for steady state simulation.

Given these temperature profiles we find that the temperature peaks at $y \approx 52$[cm] on the centerline, and the peak moves up the rod as we move radially outward. This gives the outer clad a peak temperature located at $y \approx 89$[cm]. The axial temperature profile on the outer cladding is reasonable, despite peaking closer to the top than necessarily expected. This is likely due to the relatively low mass flow rate implemented for the coolant. Generally, all of the axial temperature profiles follow the expected cosine shape indicating that our steady-state solver is likely accurate. The peak centerline temperature of roughly $T_{\max} \approx 1592$ K aligns with the results from our 1-D refinement study which found a similar value of $T_0 \approx 1590$ K with $LHR = 350 \frac{[\mathrm{W}]}{[\mathrm{cm}]}$. Any discrepancy between the two is likely due to axial diffusion of heat, as well as a different coolant temperature due to the convective cooling boundary condition.

4 Transient Simulation

To implement the transient simulation we simply scale LHR_0 by the transient equation given in the problem statement from part 1.

$$q(y,t) = \frac{\left(350 \cdot e^{-\frac{(t-20)^2}{2}} + 350\right) \cdot \cos\left(1.2 \cdot \left(\frac{y}{50} - 1\right)\right)}{0.25 \cdot \pi}$$

The transient implementation is very similar to the steady state simulation, with the addition of a time derivative kernel. In the transient simulation, we observe more dynamic behavior. In Fig. 7 we can see that the axial position of the peak temperature drops as the transient peaks. This is due to the fact that the periodicity in the cosine function defining $q(y,t)$ is constant despite a changing amplitude. This creates a higher axial thermal gradient which accelerates thermal diffusion in the axial direction. At the peak of the transient this thermal diffusion dominates the convective cooling and attracts the axial temperature profiles across the other components to the same profile as the LHR profile.

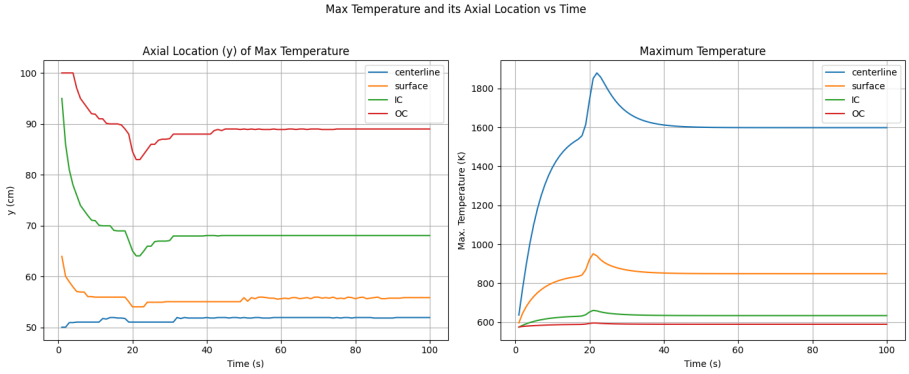

Figure 7: Plots of axial position of maximum temperature vs. time (left), and maximum temperature vs. time (right).

In the beginning of the simulation the IC, OC, and Surface of the fuel element are dominated by the convective cooling condition and due to the initial low temperature of the fuel 500 K, the convective cooling skews the temperature profile towards the top of the fuel element. 500 K was determined to be a suitable initial condition as it is the coolant inlet temperature provided in the problem statement. We also note that the widths of the minima in axial position correspond to what we might expect given the low thermal conductivity and moderately high specific heat compared to the cladding. The larger minima in axial position seen in $y(T_{\max})$ is another indicator that the simulation is accurately modeling the transient. To gain further insight into the dynamics of the temperature profile we may refer to Fig. 8. This shows us the consistent

profile that we've come to expect from analytical solutions of axial temperature profiles (quadratic across the fuel and linear in gap and clad).

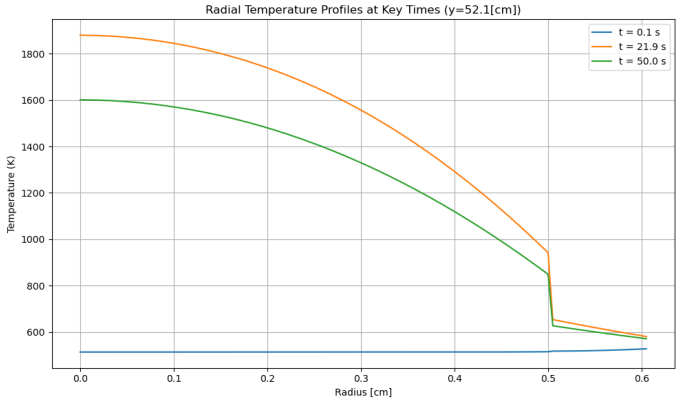

Figure 8: Radial temperature profiles at $t = 0.1, 21.9, 50$[s].

5 Integration of Solid Mechanics

To extend the model further we return to the the 1-D model from 2.2.1. Adding in necessary solid mechanics kernels to compute thermal expansion and solid mechanics properties for the mesh. This is primarily handled through the addition of stress tensors and elasticity tensors that govern material properties. These material properties are then used to handle eigenstrain calculations which model the deformation in the fuel element. The simplest modification to be made is the addition of thermal expansion to the model the material properties used are seen in 3

Material	α_{th}	E	ν
UO_2	11^{-6}	$2 \cdot 10^{10}$	0.3
Helium	0	10^2	0
Zircaloy-4	$6.6 \cdot 10^{-6}$	$9.6 \cdot 10^{10}$	0.3

Table 3: Solid state material properties for materials in the model.[2, Olander & Motta] (He values were chosen out of convenience and not a focus of this model)

After implementing solid mechanics in the model, new boundary conditions were introduced. Dirichlet boundary conditions were enforced on the left, top and bottom of the model in order to enforce that the displacements x and y

were zero. A pressure boundary condition is imposed on the right side of the model with a value of 15 MPa, this mimics actual reactor conditions. That said, the Young's modulus of the gap was chosen to be sufficiently low that this is practically equivalent to a Dirichlet BC where displacement in x is zero, prior to contact. Even so, in further extensions of the model this is a more realistic boundary condition for post-PCMI mechanics. In implementing thermal expansion convergence limits are reached with the refinement achieved in 2.2, so a new refinement was selected. As the gap nears closure the aspect ratio becomes quite narrow and slows convergence. As such a mesh-wide $n_y = 15$ was adopted across the 1-D model. Additionally, the fuel and cladding meshes were coarsened to $n_x = 20$ and the gap mesh was further refined to $n_x = 60$. This coarsening and refinement allowed the model to converge more efficiently until gap closure. In the thermal expansion model convergence was achieved up to $t_{\text{gap}} \approx 0.4\mu$m. After thermal expansion is successfully implemented we focus on incorporating burn-up dependent behaviors.

5.1 Tracking Burn-up

The burn-up in our fuel element may be analytically expressed as a function $\beta(t)$. We could track β through an analytical integral, but this is difficult and inflexible, instead we implement a Riemann sum.

To start we recognize that our volumetric heat rate $q(t)$ is in $\frac{\text{Ws}}{\text{cm}^3}$, in order to convert this to FIMA we must first gather material properties for UO_2: $\rho = 10.97\frac{\text{g}}{\text{cm}^3}$ and $\beta = 950\frac{\text{MWD}}{\text{kgU}}$, so we convert $\beta^* \left[\frac{\text{Ws}}{\text{cm}^3}\right] \rightarrow \beta \left[\frac{\text{MWD}}{\text{kgU}}\right]$

$$\frac{\beta^* \left[\frac{\text{Ws}}{\cancel{\text{cm}^3}}\right]}{\rho \left[\frac{\text{gUO}_2}{\cancel{\text{cm}^3}}\right]} = \frac{\beta^*}{10.97} \left[\frac{\cancel{W\$}}{\text{g}\cancel{\text{UO}_2}}\right] \cdot \frac{1[\text{D}]}{86400[\cancel{\$}]} \cdot \frac{1000[\text{g}\cancel{\text{UO}_2}]}{1[\text{kg}\cancel{\text{UO}_2}]} \cdot \frac{1[\text{MW}]}{10^6[\cancel{W}]} \cdot \frac{270[\text{kg}\cancel{\text{UO}_2}]}{238[\text{kgU}]} \cdot$$

$$\beta[\text{FIMA}] = 1.26 \cdot 10^{-12} \beta^* \left[\frac{\text{Ws}}{\text{cm}^3}\right]$$

The numeric integration of burn-up is compared to an analytical solution for the steady state case ($Q = 350$).

$$\beta = \frac{\dot{F}t}{N_U} = \frac{Qt}{N_U E} \approx 5.7 \cdot 10^{-10} t$$

5.2 Evolution of Material Properties

This analytical result agrees with the burn-up measured through numerical integration $\dot{\beta} = 5.615 \cdot 10^{-10}$. Having validated our burn-up calculation, we move on to the implementation of densification and swelling:

$$\epsilon_D = \min\left(-0.01, 0.01 \cdot \left(\exp\left(\frac{\beta \cdot \ln(0.01)}{\text{if}(T > 750, 1, (1, 7.235 - 0.0086 \times (T - 25)) \cdot 0.005}\right) - 1\right)\right)$$

The densification is assumed to be volumetric and the result ϵ_D is computed at every timestep and fed in to a volumetric eigenstrain material. Handling this coefficient calculation through the auxiliary system allows the densification to be tracked and output. Further auxiliary variables are added to the expression for the volumetric eigenstrain material in order to simplify the implementation and require fewer material blocks:

$$\epsilon_{\text{sfp}} = 5.577 \cdot 10^{-2} \rho_{UO_2} \beta$$
$$\epsilon_{\text{gfp}} = 1.96 \cdot 10^{-28} \rho_{UO_2} \beta (2800 - T)^{11.73} e^{-0.0162(2800-T)-17.8\rho\beta}$$

After implementing these auxiliary systems the effects of burn-up dependent properties (i.e. $\epsilon_D, \epsilon_{\text{gfp}}, \epsilon_{\text{sfp}}$) may be tracked throughout the evolution of the fuel pellet. To validate the performance of the densification and swelling models, a simulation was performed without thermal expansion(Fig. 9). We observe that

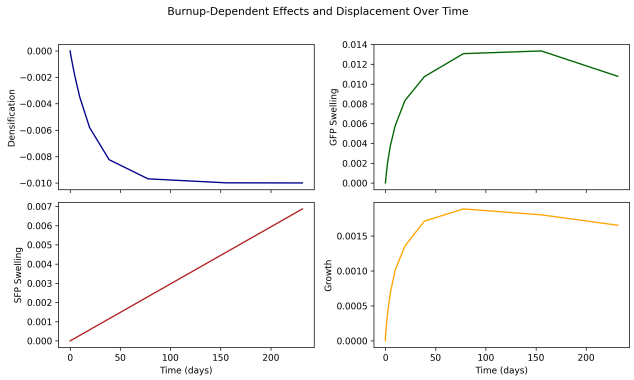

Figure 9: Behavior of burn-up dependent properties over time in simulation with no thermal expansion.

the fission product swelling and densification curves follow expected behavior. Finally, a modified Fink-Lucuta model for temperature and burn-up dependent thermal conductivity [1, 11]:

$$k(T, \beta) = \left(0.037 + 1.2 \times 10^{-4}\, T + \frac{300}{T} + 0.04\sqrt{\beta}\right)^{-1}$$

This is similar to the thermal conductivity equation used in the previous parts of the project with a burn-up degradation factor added in. A scaling factor of 0.01 was added in order to ensure agreement between this model and the values given by previous parts of the project. Given this thermal conductivity a simulation was performed until gap closure, gap closure was enforced through an iteration adaptive time-stepper, and a limiting post-processor to prevent overshooting closure. A tolerance of 0.1μm was utilized to determine closure.

In the modified Fink-Lucuta model as described gap closure was observed after roughly $2.5 \cdot 10^{-6} \frac{\text{MWd}}{\text{kgU}}$.

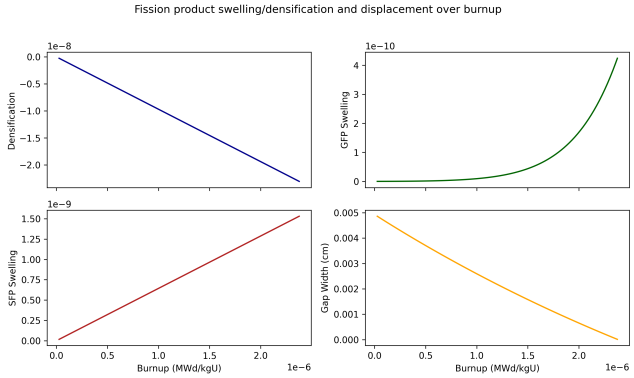

Figure 10: Behavior of burn-up dependent strains over time, and gap width until closure for $q(t) = 350$

This corresponds to roughly 4.5 seconds. In order to get more physically realistic results another simulation was performed with a sigmoid power ramp centered around 15 seconds. This provides densification a small amount of time to catch up with thermal expansion.

$$q(t) = \frac{350}{0.25\pi} \cdot \frac{1}{1 + \exp\left(-0.5\left(t - 15\right)\right)}$$

This is the benefit of numeric integration to determine burn-up, the model is easily modified to accommodate any $q(t)$. The slower ramp in fact leads to gap

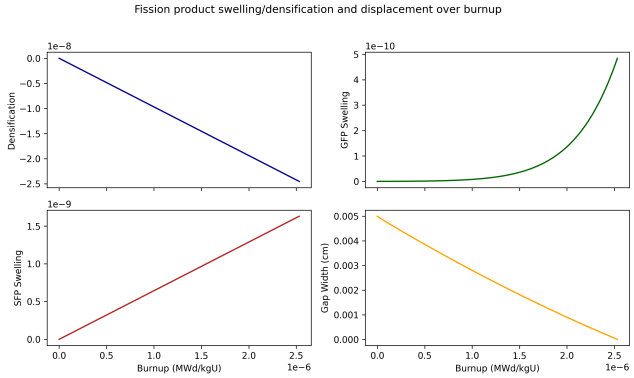

Figure 11: Behavior of burn-up dependent strains over time, and gap width until closure for sigmoid power ramp.

closure at a higher burn-up but significantly higher time (20 s). Finally, crack propagation over time was analyzed assuming $\sigma_{\text{frac}} = 100\text{MPa}$. The critical hoop stress was approximated as the vertical stress $\sigma_{\theta\theta} \approx \sigma_{yy}$, due to the

symmetry of the 1-D model. The crack front was tracked over time by finding the minimum r such that $|\sigma_{yy}(r)| > \sigma_{\text{frac}}$.

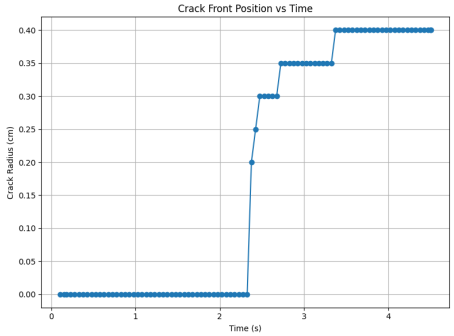

Figure 12: Calculated radius of crack front over time.

The unrealistic radius of cracking indicates that some material properties may have been poorly chosen.

6 Conclusion

Through the course of this project we have demonstrated mesh refinement studies for heat transfer in a 1-D fuel element model, a 2-D smeared pellet model, as well as the implementation of a 1-D model with solid state mechanics implemented. Future studies should focus on resolving physical inaccuracies seen, especially in the solid mechanics implementation. Poor choice of physical properties (thermal conductivity model) is likely responsible for the inaccurate cracking and stress behavior. After reconciling current model behavior with observed in-pile behavior, an extension of the solid mechanics into a 2-D smeared pellet model, or a 2-D discrete pellet model would be a valuable exercise.

The problem statement in the solid mechanics model did not allow a sufficiently slow power ramp to allow for densification and burn-up related processes to compete with the influence of thermal expansion. More realistic power ramps would be worth exploring even given the current setup. Perhaps the greatest takeaway from this project was the importance of tailoring mesh refinement to final product. The mesh refinement studies in the heat transport section of this project showed excellent convergence behavior, yet were not suitable for the solid-state mechanics portion. I think the most interesting avenue for future research is likely analytical rather than computational, focusing on relating the convergence behavior of multi-physics simulations with varying mesh properties. Such research could provide a motivated means of constructing a mesh that provides accurate results and solid convergence behavior across all physics systems in more complex simulations.

References:

1. Fink, J. K. (1989). Thermal conductivity of uranium dioxide. *Journal of Nuclear Materials, 160*(2), 251–261. https://doi.org/10.1016/0022-3115(89)90218-3

2. Oak Ridge National Laboratory. (2009). Thermophysical properties of UO_2. ORNL/TM-2009/185. https://info.ornl.gov/sites/publications/Files/Pub57523.pdf

3. International Atomic Energy Agency. (2005). Thermophysical properties of materials for water cooled reactors (IAEA-TECDOC-1496). https://www-pub.iaea.org/MTCD/publications/PDF/te_1496_web.pdf

4. Yaw, J. A. (1999). *Thermophysical properties handbook: gases and liquids* (2nd ed.). CRC Press.

5. Linstrom, P. J., & Mallard, W. G. (Eds.). (2022). *NIST Chemistry WebBook* (NIST Standard Reference Database No. 69). National Institute of Standards and Technology. https://webbook.nist.gov/chemistry/

6. Haynes, W. M. (Ed.). (2016). *CRC handbook of chemistry and physics* (97th ed.). CRC Press.

7. Garner, F. A., Greenwood, L. R., & Toloczko, M. B. (2000). *Materials handbook for fusion and fission reactor applications* (PNNL-14341). Pacific Northwest National Laboratory. https://www.pnnl.gov/main/publications/external/technical_reports/PNNL-14341.pdf

8. Incropera, F. P., DeWitt, D. P., Bergman, T. L., & Lavine, A. S. (2007). *Fundamentals of heat and mass transfer* (6th ed.). Wiley.

9. Touloukian, Y. S., et al. (1970). *Thermophysical properties of matter: The TPRC data series*. IFI/Plenum.

10. Hutton, D. V. (2004). *Fundamentals of finite element analysis*. McGraw-Hill.

11. Lucuta, P.G., Matzke, Hj., & Hastings, I.J. (1996). A pragmatic approach to modelling thermal conductivity of irradiated UO fuel: review and recommendations. Journal of Nuclear Materials, 232(2–3), 166–180.